Applied Acoustics 221 (2024) 109981

Contents lists available at ScienceDirect

Applied Acoustics

journal homepage: www.elsevier.com/locate/apacoust

Quantification of impedance and mechanical properties of Zeonor using scanning acoustic microscopy

Shivam Ojha [a], Komal Agarwal [b], Amit Shelke [a], Anowarul Habib [b,*]

[a] Department of Civil Engineering, Indian Institute of Technology Guwahati, 781039 Guwahati, Assam, India
[b] Department of Physics and Technology, UiT The Arctic University of Norway, 9037 Tromsø, Norway

ARTICLE INFO

Keywords:
Scanning acoustic microscopy
Mechanical properties
Zeonor
Impedance
Longitudinal and transversal velocity

ABSTRACT

This article explores the potential of Zeonor, a transparent cyclic olefin polymer, for applications in transparent acoustic/photo-acoustic transducers. Despite its widespread use in optics, microfluidics, medical devices, and electronics, Zeonor's acoustic properties remain understudied. To extend this, the current work employs scanning acoustic microscopy (SAM) to obtain its mechanical properties. The signal processing method known as maximal overlap discrete wavelet transform (MODWT) is applied to efficiently break down the acoustic responses of Zeonor. The filtered signal is now time-segmented to obtain the desired signal, containing the characterizing signal feature that predicts the acoustic impedance. Further, the longitudinal and transverse acoustic velocities of the Zeonor are determined using successive peak identification and time-of-flight observations. Moreover, an impedance map is developed using Kriging with a Gaussian variogram, that provides the spatial distribution of impedance. Utilizing these results, the article determines mechanical properties such as shear modulus, Young's modulus, and Poisson's ratio, finding good agreement with literature values. The lower acoustic impedance and optical transparency of Zeonor position it as an ideal material for high-frequency photo-acoustic transducers.

1. Introduction

Photoacoustic imaging, bridging optics and acoustics, is a potent non-invasive biomedical imaging technique. Leveraging the photoacoustic effect, it provides high-resolution visualization of tissue structures and functions, with applications in cancer detection, vascular imaging, and neuroscience [1–3]. Recent advancements highlight its significant potential to improve medical diagnostics and research. Optically transparent materials play a crucial role in acoustic transducers, particularly in photo-acoustic imaging (PAI) methods [4,5]. The utilization of optically transparent materials in PAI represents a pivotal advancement in the field. Optically transparent materials facilitate the effectiveness of PAI techniques by allowing light to penetrate and interact with tissues or samples, while simultaneously enabling the observation of acoustic signals. This transparency is paramount in achieving high-quality images, as it enhances the precision of light-induced acoustic wave measurements from optically absorbing structures. PAI, leveraging the merits of optical excitation and acoustic detection, generates detailed volumetric images of the samples. The strategic use of optically transparent materials in PAI not only enhances sensitivity but also expands the possibilities for applications in areas such as medical diagnostics, research, and non-invasive imaging modalities.

Despite the advantages of PAI, commercially available ultrasound transducers often use opaque backing materials, necessitating the development of transducers with a hole in the center for laser excitation of the samples [6,7]. However, this design compromises the focusing ability and sensitivity of the sensor, limiting the imaging surface and overall effectiveness [7]. A solution to this issue lies in the development of fully transparent transducers, enhancing the sensitivity of photo-acoustic imaging. Presently, transparent ultrasound transducers employ backing materials such as PMMA, epoxy (e.g., EPO-TEK 301), Lithium Niobate, and glass. The impedance of glass ceramics is 16.5 MRayl, quartz glass 13.1 MRayl, and PMMA 3.32 MRayl [8,9]. While PMMA is favored due to its lower impedance than glass and compatibility with ultrasound coupling media like water, the next generation of transducers requires optically transparent polymer substrates with lower acoustic impedance matching with water and biological tissues, low attenuation coefficients, and the ability to be produced as a thin film that can be contoured into various designs (ring-shaped, conical, spherical, etc.) [10,11]. Zeonor, an optically transparent cyclo-olefin

* Corresponding author.
E-mail address: anowarul.habib@uit.no (A. Habib).

https://doi.org/10.1016/j.apacoust.2024.109981
Received 1 December 2023; Received in revised form 4 March 2024; Accepted 16 March 2024
Available online 27 March 2024

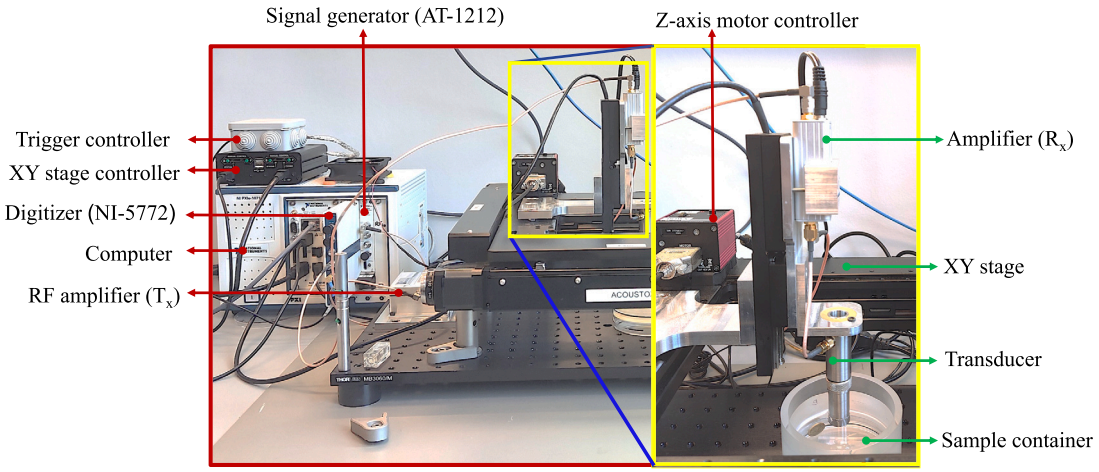

Fig. 1. The figure provides a visual representation of the SAM experimental setup, highlighting key elements such as the signal generator, XYZ translation stage, RF amplifier, receiving amplifier, digitizer, and ultrasound transducer. This visual representation serves to concisely convey the configuration of the SAM system, offering a comprehensive overview of the instrumental components involved in the image acquisition. The sample container contains samples that emerged into a coupling media (water) at room temperature for ultrasound imaging.

polymer (COP), emerges as a promising material for developing such transducers.

Zeonor possesses remarkable optical, mechanical, and thermal properties. With excellent light transmission in the visible and near-infrared regions, Zeonor exhibits flexibility, good mechanical strength, and a high glass transition temperature of 136 °C contributing to stability across a broad temperature range. It is a versatile material that can be molded or formed into thin films through plastic processing techniques [12,13]. Widely used in optical lenses, LEDs, microfluidic devices, and electronic components, Zeonor's optical clarity, ability to form thin films, moldability into various designs, and chemical resistance position it as an ideal candidate for ultrasound transducers [14–17]. However, before exploring its role in acoustic transducers, it is crucial to understand Zeonor's acoustic properties, an aspect that, to the best of our knowledge, remains unexplored. The data on the acoustic properties of Zeonor is absent from the literature.

Therefore, this article employs scanning acoustic microscopy (SAM) to determine the acoustic impedance and other mechanical properties of Zeonor. SAM provides a non-destructive and non-invasive approach for imaging materials, offering valuable quantitative data on sample thickness, acoustic wave velocities, hardness, subsurface defects, and Young's modulus [18–22]. Beyond imaging, SAM serves as a versatile technology with broad applications in mechanical characterization, subsurface evaluations, health monitoring of composite structures, defect identification in polymer circuits, and analysis of anisotropic phonon propagation [23–25]. This capability positions SAM as a valuable tool in research and development efforts related to polymer materials. Researchers can use SAM to investigate the acoustic characteristics of new polymer formulations, aiding in the development of enhanced materials with specific performance attributes. In this article, SAM is used to evaluate the acoustic properties of Zeonor, shedding light on its potential in the realm of acoustics and ultrasound applications.

In this work, we determine the acoustic impedance as well as characterize the other properties of the polymer material i.e., Zeonor. This paper discusses the methodology for the calculation of impedance and velocities briefly. For the estimation of the acoustic impedance, the acoustic response of the SAM is filtered and decomposed using maximal overlap discrete wavelet transform (MODWT) [26]. In the decomposed time series, the essential time series is selected and then time windowing is further applied to extract the required signal. This extracted signal is now transformed into a frequency domain, and a characterizing feature is selected to estimate the impedance using wave reflectance relationships. Next, successive peaks of the acoustic response are selected to estimate the longitudinal and shear velocities. The impedance and velocity maps are generated through proper interpolation [27]. Thus, utilizing the physical laws of continuum mechanics and the relationship between acoustic impedance, sound speed, and density, this methodology enables the characterization of Zeonor through acoustic response.

2. Scanning acoustic microscopic imaging

Scanning Acoustic Microscope (SAM) utilizes both reflection and transmission modes for imaging, each providing distinct insights into various aspects of the sample's properties. The image of the SAM includes annotations that emphasize its important components and operational configurations, offering a visual guide for image acquisition. The transducer concentrates acoustic energy through a commonly used coupling medium, typically water. Ultrasound signals, produced by a signal generator, are sent to the sample. When these signals bounce off the sample's surface, the returning waves are captured and converted into a digital signal, typically referred to as an A-scan or amplitude scan. To create a C-scan image of the sample, the described process is carried out multiple times by scanning at different positions within the XY plane. This means that the X-Y stage is moved to various spots on the sample's surface, acquiring data points from various locations. This collective data is then used to form a detailed image of the sample in three dimensions (X, Y, and Z), offering insights into its internal features or properties. More comprehensive explanations of the operational principles for these modes can be found somewhere else [28–30].

We designed a custom-built SAM setup as illustrated in Fig. 1 and recorded the images of the samples. This SAM system was equipped with a Standa high-precision scanning stage (8MTF-200-Motorized XY Microscope Stage) to collect experimental data. The capability for acoustic imaging was activated through the utilization of National Instruments' PXIe FPGA modules and FlexRIO hardware, which were accommodated within a PXIe chassis (PXIe-1082). The setup also included an integrated arbitrary waveform generator (AT-1212) [28,29,31]. LabVIEW program was used to operate the system. The transducer was excited with predefined Mexican hat signals and the reflected signals were amplified using an RF amplifier (AMP018032-T). Acoustic reflections originating from the sample were subsequently amplified and digitized at a high speed of 1.6 GS/s using a 12-bit digitizer (NI-5772).

We used a 30 MHz PVDF-focused Olympus transducer with particular specifications, including a 6.35 mm aperture and a 12 mm focal length, as documented in [32]. To ensure accuracy, the thickness of the PI film and Zeonor was measured using a digital micrometer, with approximate thicknesses of 130 μm and 188 μm, respectively. We scanned the samples within a scanning area of 10 mm × 2 mm, and each pixel

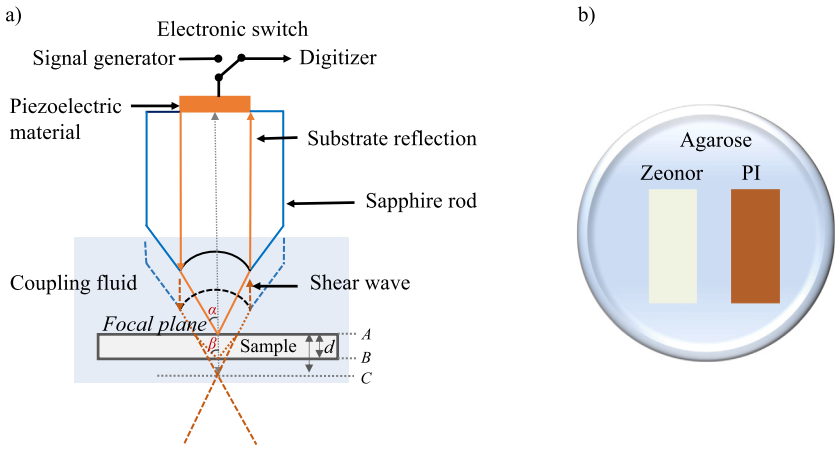

Fig. 2. a) Schematic representation of an acoustic lens with focused acoustic waves. Two types of acoustic waves are generated in the samples - longitudinal waves and shear waves, b) Schematic of sample preparation containing Zeonor and PI polymer embedded in a layer of agarose in a Petri dish. The sample container is later filled with DI water as a coupling media for SAM imaging.

represented a size of 50 μm in both the x and y dimensions. We performed scans that covered a range from 200 μm above to 800 μm below the focal point of the thickest sample (Zeonor), using a step size of 20 μm (see Fig. 2 (a). This meticulous approach was taken to guarantee that both the samples, regardless of their varying thicknesses, were imaged at their focal planes as depicted in Fig. 2 (a). Additionally, it allowed us to obtain z-scans of the samples at various depths, ensuring comprehensive data acquisition.

The samples were prepared by embedding samples in an agarose gel. A 2 wt% agarose solution (Sigma Aldrich) was formulated by dissolving it in distilled water at 100 °C with the aid of a magnetic stirrer. Subsequently, a thick gel layer was poured onto a standard Petri dish (μ-Dish 35 mm from ibidi). On top of the gel, the Zeonor sample and the control sample Polyimide (PI) were gently pressed, incorporating them into the gel matrix. A visual representation of this sample preparation process is depicted in Fig. 2(b). For SAM imaging, distilled water was meticulously introduced into the Petri dish. Utilizing agarose, which has an impedance similar to water, served to stabilize the samples during imaging [33]. This methodology facilitated the simultaneous capture of images for all samples in a single session.

3. Proposed methodology for material characterization

The present study employs two distinct methodologies to assess acoustic impedance and characterize velocity. Zeonor material exhibits both longitudinal and shear velocity. The foundational principles of acoustic wave behavior in scanning acoustic microscopy serve as the underpinning for both methodologies. The incident wave of the acoustic P-wave generates four distinct wave components, namely, a) reflected P wave (RPP), b) reflected S wave (RPS), c) transmitted P wave (TPP), and d) transmitted S wave (TPS). Assigning the wavenumbers to different wave components, the reflectance R_{PP} for the normal incidence is provided by the following equation [34]:

$$R_{PP} = \frac{k_{P1}k_{S2}^2\mu_{21} - k_{P2}k_{S1}^2}{k_{P1}k_{S2}^2\mu_{21} + k_{P2}k_{S1}^2} = \frac{Z_2 - Z_1}{Z_2 + Z_1} \tag{1}$$

where, $k_{P1}, k_{P2}, k_{S1}, k_{S2}$ are the wavenumbers of P and S waves traveling in material 1 and 2 (in our case, material 1 will be either Polyimide/Zeonor and material 2 will be glass), and $\mu_{21} = \mu_2/\mu_1$ is the ratio of Lamé constants. Further, Z_1 and Z_2 are the acoustic impedance. Here, we are solving the inverse problem where the reflectance and the impedance need to be estimated from acoustic responses. Let the characterization frequency of the transmitted, reflected signal through reference and target medium be S_0, S_{ref} and S_{target}, respectively [35]. The following relationship can be written: [34–37]

$$S_{\text{target}} = \frac{Z_{\text{target}} - Z_{\text{sub}}}{Z_{\text{target}} + Z_{\text{sub}}} S_0,\ S_{ref} = \frac{Z_{ref} - Z_{sub}}{Z_{ref} + Z_{sub}} S_0 \tag{2}$$

where Z_{target}, Z_{ref}, and Z_{sub} represent the acoustic impedance of the target, reference, and substrate, respectively. Let $S_r = \frac{S_{target}}{S_{ref}}$, and $R_{ref} = \frac{Z_{ref} - Z_{sub}}{Z_{ref} - Z_{sub}}$, the acoustic impedance of the target medium is subsequently given by:

$$Z_{target} = \frac{1 + S_r \cdot R_{ref}}{1 - S_r \cdot R_{ref}} Z_{sub} \tag{3}$$

Moreover, due to various interfaces, the reflected response of the acoustic imaging contains multiple peaks having different frequency components that are transmitted and reflected through the various interfaces resulting in the formulation of a time-frequency analysis problem. However, the dominant characteristic part will show the highest peak in the power spectrum. The response is initially filtered through the bandpass filter to remove unwanted noise and then maximal overlap discrete wavelet transform (MODWT) is applied to decompose the signal into multiple time series having its own wavelet and scaling coefficients for different levels [26,38,39]. Moreover, Mallat's algorithm is applied in implementing MODWT practically. This algorithm incorporates a set of filters, including a low-pass filter (scaling function) and a high-pass filter (wavelet function). MODWT can be accurately defined for signals of arbitrary length and achieves redundancy through an oversampled representation, allowing for more precise statistical analysis [38]. Let $X = X_t, t = 0, ..., T-1$, be the time series data, then, the j$^{\text{th}}$ level wavelet and scaling filters are denoted as $\{\tilde{h}_{jl}\}$ and $\{\tilde{g}_{jl}\}$, respectively. The scaling and wavelet coefficients calculated by Mallat's algorithm are described as follows:

$$\tilde{W}_{j,t} = \sum_{l=0}^{T-1} \tilde{h}_{j,l} X_{t-l \bmod T},\ \tilde{V}_{j,t} = \sum_{l=0}^{T-1} \tilde{g}_{j,l} X_{t-l \bmod T} \tag{4}$$

where $j = 1, 2, ..., J_0$ is the level of wavelet decomposition, and 'mod' denotes the remainder of dividing two numbers. The wavelet $\dot{\boldsymbol{W}}_j$ and scaling $\tilde{\boldsymbol{V}}_j$ coefficients vectors of MODWT are written as:

$$\dot{\boldsymbol{W}}_j = \left\{\tilde{W}_{j,0}, \tilde{W}_{j,1}, \ldots, W_{j,T-1}\right\}, j = 1, 2, \ldots, J_0 \tag{5}$$

$$\tilde{\boldsymbol{V}}_j = \left\{\tilde{V}_{j,0}, \tilde{V}_{j,1}, \ldots, \tilde{V}_{j,T-1}\right\}, j = 1, 2, \ldots, J_0, \tag{6}$$

where $\tilde{\boldsymbol{V}}_j$ and $\dot{\boldsymbol{W}}_j$ are related to the smallest and highest frequency components of the original signal. $\{\tilde{h}_{j,l}\}$, and $\{\tilde{g}_{j,l}\}$ are the j$^{\text{th}}$ level MODWT high-pass filter $\left(\tilde{h}_{j,l} \equiv h_{j,l}/2^{j/2}\right)$ and low-pass filter $\left(\tilde{g}_{j,l} \equiv g_{j,l}/2^{j/2}\right)$ and J_0 is the highest decomposition level. For the level

3 decomposition, the MODWT decomposes an original signal X into a low-pass filtered approximation component (A_3) and high-pass filtered detail components $(D_1, D_2 \text{ and } D_3)$. The equations of MODWT-based multi-resolution analysis can be used for the reconstruction of decomposed signal and are written as follows:

$$\mathbf{X} = \sum_{j=1}^{L} D_j + A_{J_0}, \quad D_{j,t} = \sum_{l=0}^{n-1} \tilde{h}_{j,l} W_{j,t+l \bmod n} \tag{7}$$

By employing the aforementioned equations, the signal is reconstructed at each decomposition level. These decomposed signals undergo reconstruction through the application of inverse wavelet transform (iMODWT), utilizing the wavelet coefficients associated with the desired levels. Subsequently, the power of each decomposed time series is computed and normalized against the maximum power. This process enables the selection of the essential time series, identified as the one with the highest power relative to others. Once the essential time series is selected, a time window of time interval 0.25 ns is considered and the signal is extracted. The time-windowing is important to accurately focus on the desired signal characteristics. Thus the extracted window is then transformed into the frequency domain and the power spectrum is observed. The frequency at which the power spectrum achieves the peak value is considered the characteristic feature of the response and is used in the calculation of acoustic impedance. Since the time windowing is a manual process, the impedance is first calculated at randomly spread selected points sampled using Latin hypercube sampling, and then Kriging using a Gaussian variogram is performed to find the impedance over the complete domain [27,40,41].

The next step involves determining the longitudinal and shear velocities of Zeonor. Rayleigh, longitudinal, and shear waves are produced by the transducer at the interface between the fluid and the sample. These sound waves undergo reflection at both the front and rear surfaces of the Zeonor film, subsequently traveling back to the transducer. The refraction of these waves is determined by Snell's law. Raum et al. and Hänel derived the mathematical equations to determine the longitudinal velocity, and shear velocity as described below [42–44]. When acoustic waves are directed toward the front surface of the sample, the time of flight TOF_1 can be observed and is given as:

$$TOF_1 = \frac{2F}{v_0} \tag{8}$$

where v_0 is the speed of sound in the coupling fluid and F is the focal distance. When the transducer is moved further down closer to the sample, both the shear and longitudinal waves will now focus on the rear surface. This results in transit time TOF_2 of the longitudinal wave with the angle of incidence α in the sound field and is given by:

$$TOF_2 = \frac{2F}{v_0} - \frac{2U_T}{v_0 cos\alpha} + \frac{2U_T \cdot v_0}{v_1^2 cos\alpha} \tag{9}$$

where U_T is the transducer displacement needed to focus on the rear surface from the front. The sound velocity is then determined by Eq. (10), as shown below [43]:

$$v_l = \sqrt{{v_0}^2 / \left(1 - \frac{(TOF_1 - TOF_2) \cdot v_0 \cdot cos\alpha}{2U_T}\right)} \tag{10}$$

When the shear wave is focused on the rear side, lateral stress components are extinguished and the remaining normal stress components generate a longitudinal wave. The time of flight of this reflected pulse is:

$$TOF_3 = \frac{2F}{v_0} - \frac{2U_T}{v_0 \cos\alpha} + \frac{d}{v_1 \cos\beta_s} + \frac{d}{v_s \cos\beta_s} \tag{11}$$

where as U_T is the transducer displacement to focus from the front surface to the rear shear wave focus, d is equal to the sample thickness, and β_s is the angle of refraction. The shear wave velocity is obtained from:

Table 1
It presents equations for the estimation of various important parameters for the characterization of Zeonor.

Parameter	Formula
Density:	$\rho = \frac{Z}{v_l}$
Stiffness:	$c_{11} = Z \cdot v_l$
Shear modulus:	$c_{44} = \rho \cdot v_s^2$
Bulk modulus:	$B = c_{11} - \frac{4}{3} c_{44}$
Young's modulus:	$E = c_{44} \cdot \frac{3c_{11} - 4c_{44}}{c_{11} - c_{44}}$
Poisson's ratio:	$\sigma = \frac{1 - 2c_{44}/c_{11}}{2(1 - 2c_{44}/c_{11})}$

$$v_s = d \Big/ \left(\cos\beta_s \left[\frac{2U_T}{v_0 \cdot \cos\alpha} - \frac{d}{v_l \cdot \cos\beta_s} - (TOF_1 - TOF_3)\right]\right) \tag{12}$$

Once, the impedance and velocities are predicted, later on, complete characterization is done using the equation presented in Table 1.

4. Results and discussion

To characterize Zeonor material, two distinct methodologies are employed to estimate acoustic impedance and wave velocities. The acoustic properties are analyzed through an experiment utilizing scanning acoustic microscopy (SAM) on a 188 μm thick Zeonor sample. The response is recorded at various spatial and plane locations across the thickness. The response signal exhibits multiple frequency bands, predominantly ranging from 20 MHz to 40 MHz with temporal spread. To better comprehend the signal's characteristics, the time-frequency plot is initially examined using the short-term Fourier transform (STFT) and subsequently decomposed using the MODWT. Fig. 3(a) thoughtfully presents the visual representation of these frequencies after band-pass filtering, offering insight into the signal's frequency content and aiding in understanding the changes in the system's acoustic response over time.

The MODWT decomposed the signal into several time series based on the different levels of the wavelet coefficients. To reconstruct the filtered signal, the power of each decomposed time series is computed and normalized against the maximum power. The time series that has maximum energy content is selected as the essential time series and considered as the filtered signal as represented in Figs. 3(b). It provides a clear distinction and changes that are observed in the filtered responses due to the removal of unwanted frequencies from the signal through the MODWT.

Once the essential time series is selected, a time window with a time interval of 0.25 μs is considered, as depicted in Fig. 4(a) and (b). The signal is then extracted from the point where the power spectrum reaches its maximum peak. The time domain responses of the extracted signal for Zeonor and Polyimide are displayed in Fig. 4(c) and (d). The frequency at which the power spectrum achieves its peak value is considered a characteristic feature of the response and is utilized to calculate acoustic impedance. As outlined in the theory section, the characteristic feature S_{ratio} necessitates a reference medium for impedance estimation, which in our study is Polyimide (PI). This extracted signal is transformed into the frequency domain, and the power spectrum curve is illustrated in Fig. 4(e) and (f). The corresponding spectrogram for the Zeonor and PI samples is presented in Fig. 4(g) and (h). The fundamental frequencies are correlated to the material, aiding in deducing the reflectance property associated with the medium, ultimately providing the impedance of the Zeonor through the earlier described procedure.

The spatial distribution of the measured impedance at a specific plane is illustrated in Fig. 5(a). The specific acoustic impedance values lie in the range from 2.67 to 2.71 Mrayl, representing variations across the plotted area. This information offers insights into the localized impedance characteristics of the Zeonor. The ratio S_{ref} is calculated for different positions of the image plane across the thickness, and the corresponding impedance values are presented in Figs. 5(b) and (c).

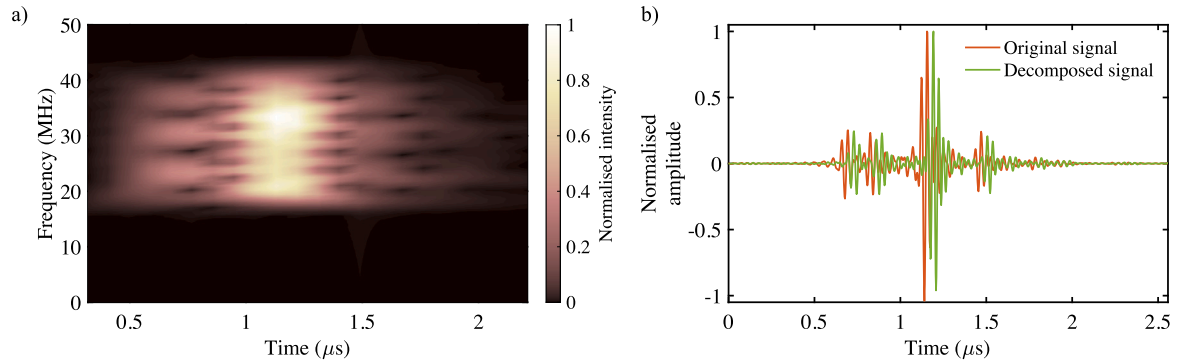

Fig. 3. (a) It represents the short-term frequency transform of the acoustic response of Zeonor. (b)It illustrates both the original and MODWT decomposed responses of the signal. The original signal from Zeonor is highlighted in red, while the decomposed signal is represented in green.

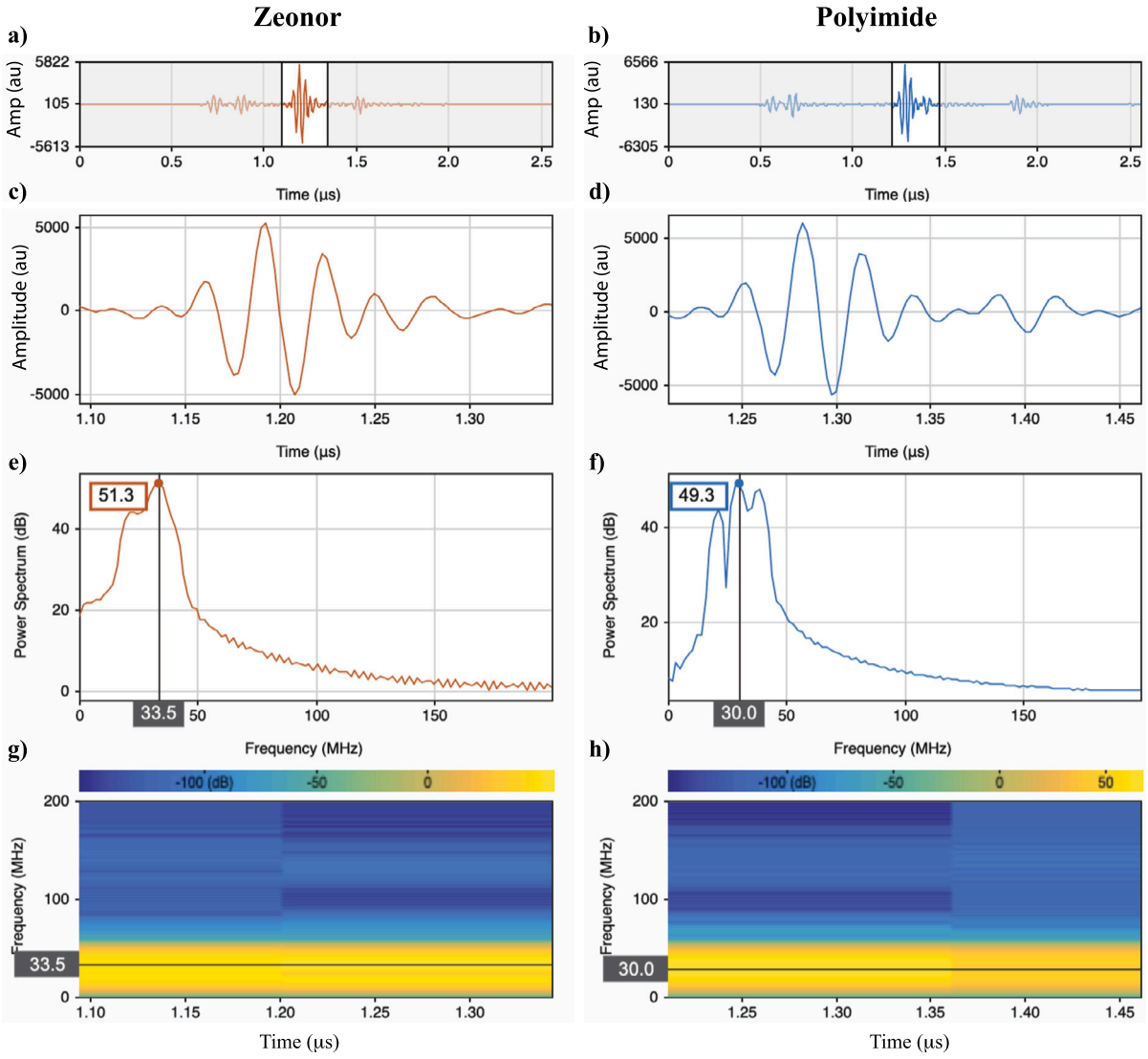

Fig. 4. It demonstrates the operations that are carried out after the essential time series is selected. The time-window of interval 0.25 μs is selected as represented in figures (a) and (b). The figures (c) and (d) represent the extracted signal. This extracted signal is now transformed into the frequency domain, and the power spectrum curve is shown in Figures (e) and (f). Further, figures (g) and (h) represent the spectrogram for the Zeonor and Polyimide (PI), respectively.

It can be noted that the mean value of the specific acoustic impedance across the thickness and space is found to be 2.69 Mrayl with a standard deviation of 0.03. Once the impedance is found, the next step is to estimate the longitudinal and shear velocities of the Zeonor medium using peak amplitude and corresponding time interval obtained from the acoustic response. It should be noted that multiple reflections are associated with different amplitude peaks in the same signal. The normalized amplitude and the time of flight at each position of the image plane across thickness are presented in Fig. 6 (a) and (b) respectively. As described in the theory section, TOF_1 can be calculated,

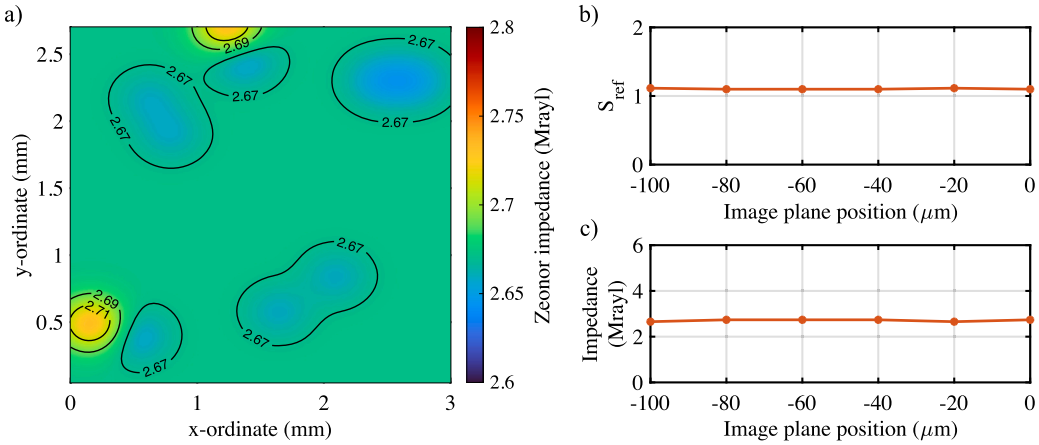

Fig. 5. (a) Spatial mapping of the acoustic impedance on Zeonor represents how the acoustic impedance is distributed across a specific plane, providing insight into the spatial variations of this acoustic property. (b) The depiction of S_{ref} variation across the thickness illustrates changes in the reflection coefficient throughout the material's thickness. Figure (c) illustrates the variation of the acoustic impedance across the thickness, representing how the acoustic impedance values change throughout the material's thickness.

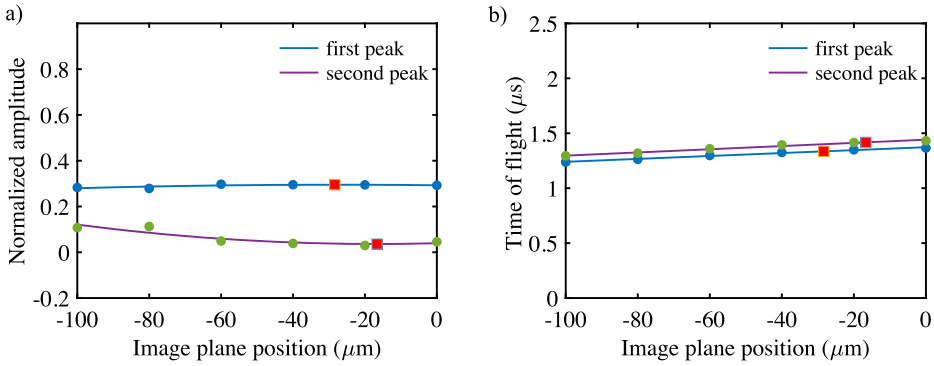

Fig. 6. (a) Representation of the normalized amplitude of the acoustic responses across the thickness of the specimen. It has two curves representing the value for the first peak and the second peak in the signal. (b) illustrates the time of flight for the two peaks of the signal.

Table 2
Material properties obtained for the Zeonor.

Description	Mean	Units
Impedance (Z)	2.69	Mrayl
Longitudinal velocity (v_l)	2590	m/s
Shear velocity (v_s)	1160	m/s
Density (ρ)	1.03	g/cm^3
Stiffness modulus (c_{11})	6.97	GPa
Shear Modulus (c_{44})	1.40	GPa
Bulk Modulus (B)	5.10	GPa
Young's Modulus (E)	3.84	GPa
Poisson's ratio (σ)	0.37	-

TOF_2 and TOF_3 can be estimated from the time of flight observed for the front and rear refection causing the first and second peaks as provided in Fig. 6(b). Once the TOF_1, TOF_2, and TOF_3 are estimated, and we have the values of speed of sound and transducer displacement, the longitudinal and shear velocities are calculated. For brevity purposes, the result for the nominal location is presented here. The longitudinal velocity and transverse/shear velocity of Zeonor were determined to be (2590 ± 32) m/s and (1152 ± 28) m/s, respectively. Utilizing these velocity values along with the impedance, Zeonor was further characterized using the mathematical formulae stated in Table 1. Mechanical properties of Zeonor are summarized in Table 2. The density of Zeonor was measured at $1.03 g/cm^3$, aligning closely with literature-reported values [45]. The observed tensile modulus of Zeonor, measured at approximately 3.8 GPa, deviates significantly, by about 0.8 GPa, from the values reported in the existing literature [45]. Several factors could contribute to this notable disparity. Firstly, the composition of Zeonor may play a crucial role. Variations in the chemical composition, molecular structure, or additives within the material can influence its mechanical properties. Differences in the manufacturing process, such as variations in raw material quality or formulation, might contribute to this discrepancy. Secondly, the processing parameters employed during sheet production could impact the tensile modulus. Factors such as temperature, pressure, and processing duration during the fabrication of Zeonor sheets can influence its mechanical characteristics. Variations in these parameters might lead to differences in the material's response to tensile stress. Additionally, the calculated longitudinal and transverse velocities, used in the characterization of Zeonor, may introduce uncertainty. If there are deviations or uncertainties in these velocity values, they could propagate into the calculation of the tensile modulus, contributing to the observed variation.

5. Conclusion

In conclusion, Zeonor, a transparent cyclic olefin polymer, emerges as a promising material for flexible and transparent transducers for photo-acoustic imaging. This research, focused on characterizing Zeonor through scanning acoustic microscopy, elucidates its acoustic properties, such as impedance, longitudinal, and transverse/shear velocities. These acoustic values were further used to derive mechanical properties, such as Young's modulus, stiffness, shear modulus, and bulk modulus of the Zeonor polymer. A notable advantage lies in Zeonor's

lower impedance compared to alternative transducer fabrication materials like glass, sapphire, Polyetherimide, and PMMA. The measured specific impedance value of 2.69 Mrayl for Zeonor signifies its well-suited nature for applications as a flexible and transparent transducer. The acoustic characteristics not only validate Zeonor's compatibility but also accentuate its effectiveness, particularly in acoustic and photoacoustic imaging. Additionally, the calculated mechanical properties exhibit strong agreement with existing literature, affirming the reliability of our findings and further emphasizing Zeonor's potential in transducer development.

CRediT authorship contribution statement

Shivam Ojha: Writing – original draft, Formal analysis, Conceptualization. **Komal Agarwal:** Writing – review & editing, Writing – original draft, Data curation. **Amit Shelke:** Writing – review & editing, Supervision, Conceptualization. **Anowarul Habib:** Writing – review & editing, Supervision, Funding acquisition, Data curation, Conceptualization.

Declaration of competing interest

The authors declare that they have no known competing financial interests or personal relationships that could have appeared to influence the work reported in this paper.

Data availability

Data will be made available on request.

Acknowledgement

This work was supported by the Research Council of Norway, Cristin Project, ID: 2061348.

References

[1] Wood CA, et al. Clinically translatable quantitative molecular photoacoustic imaging with liposome-encapsulated icg j-aggregates. Nat Commun 2021;12:5410.
[2] Ghosh B, Chatterjee J. Advances in medical imaging for wound repair and regenerative medicine. In: Regenerative medicine: emerging techniques to translation approaches. Springer; 2023. p. 57–76.
[3] Ghosh B, Agarwal K. Viewing life without labels under optical microscopes. Commun Biol 2023;6:559.
[4] Manwar R, Avanaki K. Manufacturing process of optically transparent ultrasound transducer: a review. IEEE Sens J 2023.
[5] Ren D, Sun Y, Shi J, Chen R. A review of transparent sensors for photoacoustic imaging applications. In: Photonics, vol. 8. MDPI; 2021. p. 324.
[6] Wong TT, et al. Label-free automated three-dimensional imaging of whole organs by microtomy-assisted photoacoustic microscopy. Nat Commun 2017;8:1386.
[7] Plakke A. Transparent transducer for photoacoustic imaging: making a 2x2 array using pvdf coated with ito; 2022.
[8] Gao W, Liu W, Hu Y, Wang J. Study of ultrasonic near-field region in ultrasonic liquid-level monitoring system. Micromachines 2020;11:763.
[9] Xia W, Piras D, van Hespen JC, Steenbergen W, Manohar S. A new acoustic lens material for large area detectors in photoacoustic breast tomography. Photoacoustics 2013;1:9–18.
[10] Gómez TE, et al. Low-impedance and low-loss customized materials for air-coupled piezoelectric transducers. In: 2001 IEEE ultrasonics symposium. Proceedings. An international symposium (Cat. No. 01CH37263), vol. 2. IEEE; 2001. p. 1077–80.
[11] Rhee S, Ritter T, Shung K, Wang H, Cao W. Materials for acoustic matching in ultrasound transducers. In: 2001 IEEE ultrasonics symposium. Proceedings. An international symposium (Cat. No. 01CH37263), vol. 2. IEEE; 2001. p. 1051–5.
[12] Yang J, Choi S, Kim C. Practical review on photoacoustic computed tomography using curved ultrasound array transducer. Biomed Eng Lett 2022:1–17.
[13] Yao J, Wang LV. Sensitivity of photoacoustic microscopy. Photoacoustics 2014;2:87–101.
[14] Shinoj V, Murukeshan V, Tor S, Loh N, Lye S. Design, fabrication, and characterization of thermoplastic microlenses for fiber-optic probe imaging. Appl Opt 2014;53:1083–8.
[15] Gubala V, et al. Simple approach to study biomolecule adsorption in polymeric microfluidic channels. Anal Chim Acta 2013;760:75–82.
[16] Teffer AK, et al. A molecular assessment of infectious agents carried by Atlantic salmon at sea and in three eastern Canadian rivers, including aquaculture escapees and North American and European origin wild stocks. Facets 2020;5:234–63.
[17] Ferraro A, Zografopoulos DC, Caputo R, Beccherelli R. Broad- and narrow-line terahertz filtering in frequency-selective surfaces patterned on thin low-loss polymer substrates. IEEE J Sel Top Quantum Electron 2017;23:1–8.
[18] Briggs A, Kolosov O. Acoustic microscopy, vol. 67. Oxford University Press; 2010.
[19] Habib A, et al. Mechanical characterization of sintered piezo-electric ceramic material using scanning acoustic microscope. Ultrasonics 2012;52:989–95.
[20] Brand S, et al. Extending acoustic microscopy for comprehensive failure analysis applications. J Mater Sci, Mater Electron 2011;22:1580–93.
[21] Habib A, et al. Quantitative ultrasonic characterization of c-axis oriented polycrystalline aln thin film for smart device application. Acta Acust Acust 2015;101:675–83.
[22] Agarwal K, Habib A, Dalmo RA, Olukan TA, Melandsø F. Acoustic velocity estimation of salmon fish scales using acoustic microscope. In: 2023 IEEE International Ultrasonics Symposium (IUS). IEEE; 2023. p. 1–4.
[23] Yu H. Scanning acoustic microscopy for material evaluation. Appl Microsc 2020;50:1–11.
[24] Wagle S, Habib A, Melandsø F. Ultrasonic measurements of surface defects on flexible circuits using high-frequency focused polymer transducers. Jpn J Appl Phys 2017;56:07JC05.
[25] Morokov ES, et al. Noninvasive high-frequency acoustic microscopy for 3d visualization of microstructure and estimation of elastic properties during hydrolytic degradation of lactide and ε-caprolactone polymers. Acta Biomater 2020;109:61–72.
[26] Cornish CR, Bretherton CS, Percival DB. Maximal overlap wavelet statistical analysis with application to atmospheric turbulence. Bound-Layer Meteorol 2006;119:339–74.
[27] Rasmussen CE, Williams CK, et al. Gaussian processes for machine learning, vol. 1. Springer; 2006.
[28] Kumar P, et al. Numerical method for tilt compensation in scanning acoustic microscopy. Measurement 2022;187:110306.
[29] Gupta SK, Pal R, Ahmad A, Melandsø F, Habib A. Image denoising in acoustic microscopy using block-matching and 4d filter. Sci Rep 2023;13:13212.
[30] Somani A, et al. Image inpainting with hypergraphs for resolution improvement in scanning acoustic microscopy. In: Proceedings of the IEEE/CVF conference on computer vision and pattern recognition; 2023. p. 3112–21.
[31] Gupta SK, Habib A, Kumar P, Melandsø F, Ahmad A. Automated tilt compensation in acoustic microscopy. J Microsc 2023.
[32] Olympus. Polymer (pvdf) immersion transducers. Available from: https://www.olympus-ims.com/data/File/panametrics/panametrics-UT.en.pdf, 2010.
[33] Dong E, et al. Bioinspired metagel with broadband tunable impedance matching. Sci Adv 2020;6:eabb3641.
[34] Kundu T. Mechanics of elastic waves and ultrasonic nondestructive evaluation. CRC Press; 2019.
[35] Prastika EB, et al. Time and frequency domain deconvolution for cross-sectional cultured cell observation using an acoustic impedance microscope. Ultrasonics 2022;119:106601.
[36] Cheeke JDN. Fundamentals and applications of ultrasonic waves. CRC Press; 2017.
[37] Kobayashi K, Yoshida S, Saijo Y, Hozumi N. Acoustic impedance microscopy for biological tissue characterization. Ultrasonics 2014;54:1922–8.
[38] Percival DB, Walden AT. Wavelet methods for time series analysis, vol. 4. Cambridge University Press; 2000.
[39] Nason GP. Wavelet methods in statistics with R. Springer; 2008.
[40] Cressie N. The origins of kriging. Math Geol 1990;22:239–52.
[41] Schulz E, Speekenbrink M, Krause A. A tutorial on Gaussian process regression: modelling, exploring, and exploiting functions. J Math Psychol 2018;85:1–16.
[42] Raum K. Quantitative akustische rastermikroskopiemethoden zur charakterisierung der elastischen eigenschaften von knochengewebe. Diss. Martin-Luther-Universität Halle-Wittenberg; 2002.
[43] Raum K, Brandt J. Simultaneous determination of acoustic impedance, longitudinal and lateral wave velocities for the characterization of the elastic microstructure of cortical bone. In: Proceedings WCU 2003; 2003. p. 321–4.
[44] Hänel V. Measurement of sound velocity and thickness of thin samples by time-resolved acoustic microscopy. J Appl Phys 1998;84:668–70.
[45] Zeon C. Cyclo olefin polymer zeonex. Available from: https://www.zeon.co.jp/en/business/enterprise/resin/pdf/200323391.pdf, 2023.